ELSEVIER

Contents lists available at ScienceDirect

Journal of Colloid and Interface Science

journal homepage: www.elsevier.com/locate/jcis



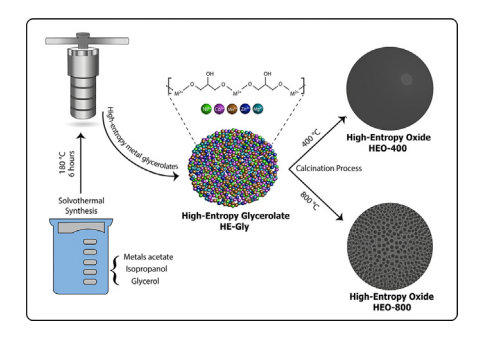
Multimetallic glycerolate as a precursor template of spherical porous high-entropy oxide microparticles



Josué M. Gonçalves ^{a,b,*}, Alireza Ghorbani ^a, Timothy G. Ritter ^c, Irlan S. Lima ^b, Mahmoud Tamadoni Saray ^a, Abhijit H. Phakatkar ^d, Vinicius D. Silva ^a, Rafael S. Pereira ^e, Alexander L. Yarin ^a, Lúcio Angnes ^b, Reza Shahbazian-Yassar ^{a,*}

- ^a Department of Mechanical & Industrial Engineering, University of Illinois at Chicago, Chicago, IL 60607, USA
- ^b Instituto de Química, Universidade de São Paulo, Av. Prof. Lineu Prestes 748, 05508-000 São Paulo-SP, Brazil
- ^cDepartment of Civil & Materials Engineering, University of Illinois at Chicago, Chicago, IL 60607, USA
- ^d Department of Biomedical Engineering, University of Illinois at Chicago, Chicago, IL 60607, USA

G R A P H I C A L A B S T R A C T



ARTICLE INFO

Article history: Received 22 November 2022 Revised 6 March 2023 Accepted 13 March 2023 Available online 17 March 2023

Keywords: High-Entropy Coordination Compound High-Entropy Metal-Glycerolate High-Entropy Oxides Spinel Phase

ABSTRACT

High-entropy materials have received notable attention concern on account of their unique structure, tunable properties, and unprecedented potential applications in many fields. In this work, for the first time a NiCoMnZnMg-containing high-entropy glycerolate (HE-Gly) particles has been synthesized using a scalable solvothermal method. The HE-Gly particles were used as a precursor in design of porous high-entropy oxide (HEO) microparticles. The morphological and structural characterizations demonstrate that the temperature of the annealing process, and the composition of the metal ions in the HE-Gly precursors play important roles in determining porosity, crystallinity, and phase separation in HEOs. In fact, HE-Gly exhibited a porous structure of spinel HEOs with secreted MgO phase after annealing process at 800 °C, while the annealing process at 400 °C led to a low-crystallinity spinel phase without phase segregation. Overall, this work describes HE-Gly as a new precursor for altering the composition, crystallinity, and porosity of HEOs. This strategy is scalable for potential high mass productions, paving a new path toward industrial application of high-entropy materials.

© 2023 Elsevier Inc. All rights reserved.

E-mail addresses: rsyassar@uic.edu (J.M. Gonçalves), josuefisicoquimico@hotmail.com (R. Shahbazian-Yassar).

1. Introduction

Recently, high-entropy materials (HEMs) attracted significant attention in relation to different applications, such as coating [1],

^e Centro de Engenharia, Modelagem e Ciências Sociais Aplicadas, Universidade Federal do ABC, 09210-580 Santo André, SP, Brazil

^{*} Corresponding authors at: Department of Mechanical &Industrial Engineering, University of Illinois at Chicago, Chicago, IL 60607, USA.

refractory materials [2], healthcare items [3], sensors [4], electrocatalysis [5], and especially as electrode materials for energy conversion and storage [6]. In fact, the concept of HEMs is based on entropy stabilization of crystal structure resulting in random distribution of elements in a solid solution phase [7]. It has been suggested that five or more different elements are essential to overcome the enthalpy of intermetallic formations or phase separation [8]. There is significant interest in HEMs due to their novel and often unexpected and unprecedented properties [9].

In a few years, a variety of HEMs were reported in literature, such as high-entropy alloys (HEAs), high-entropy oxides (HEOs), high-entropy hydroxides (HEHs), and many others, which have been utilized in a broad range of applications. More recently, the library of HEMs was further expanded, and the concept of high entropy was introduced into some coordination compounds such Prussian blue analogues (PBAs) [10] and other metal-organic frameworks (MOFs) [11], as well as metal-glycerate/metal-glycero lates which may facilitate new opportunities in electrochemical applications [12]. For instance, Ma *et al.* [10] have demonstrated that high-entropy versions of PBA (HE-PBA) cathode materials may reveal a substantially improvement in the electrochemical performance for sodium storage. According to the authors, the key to such improvement lies in the high entropy and associated effects, as well as the presence of several active redox centers.

Interestingly, amorphous high-entropy glycerolates (HE-Glys) have been synthesized using a scalable solvothermal method [13]. The noble metal-free HE-Gly containing five different metals (Fe, Ni, Co, Cr, and Mn) was found to be more active than its subsystems of quadri-, tri-, and bimetallic glycerolates [13]. In fact, the synergistic interactions among the metal elements with peculiar electronic structure and coordination environment result in excellent catalytic activity, while the electrochemical stability is ascribed to the high-entropy configuration effect [13]. However, it should be emphasized that these multimetallic coordination compounds have a high-entropy configuration, albeit are generally not entropy-stabilized.

Despite the attractive properties of HE-Gly (and HE-MOFs), HE-Gly materials only partially meet the requirements as advanced materials for electrochemical application [12]. In fact, realistic applications of HE-Gly in electrode materials are strongly dependent on such essential features as the electrical conductivity and design of redox-active sites for satisfactory performance [12,14]. In this context, and aiming to circumvent this problem, the use of metal-glycerolate (or MOFs) as sacrificial templates/precursors for design of micro/nanomaterials holds great promise [14], exhibiting exceptional conductivity, electrochemical activity, stability, a desired composition and porous structure. Currently, metal-glycerolate-derived materials were reported as excellent precursors/templates for preparation of many mono- and bimetallic versatile and multifunctional porous metal oxides, metal hydroxides, metal sulfides, metal phosphides and metal phosphates with homogeneous structures [12,15]. In fact, compared with MOFs, the proportion of metal ions in metal-glycerolate spheres is much higher, which can result in nanocrystalline metal-glycerolate-derived materials with much higher metal concentration and more stable structures that can resist oxidation without any structural deterioration [12]. In addition, it is important to highlight that there is a great interest for the development of new products derived from glycerol, which is a biobased, widely available, being a coproduct from the biodiesel industry [12].

In this study, it is proven that a chosen composition and heattreatment temperature can play an important role in design of new HEOs derived from unprecedented HE-Gly. The temperature of the annealing process plays an important role in development of porosity and crystallinity of the prepared HEOs, which is demonstrated by morphological and structural characterization. The presence of Mg²⁺ is used here for the first time in the form of highentropy NiCoMnZnMg-glycerolate. This strategy can be key in the development of strategic and desirable HEOs compositions for different future applications, opening a new path toward synthesizing high-entropy materials.

2. Experimental

2.1. Chemicals

All the chemicals were directly used as received without further purification. Glycerin, isopropyl alcohol, and nickel acetate tetrahydrate (Ni(CH₃COO)₂·4H₂O) were purchased from Sigma–Aldrich. Anhydrous ethyl alcohol was purchased from KOPTEC. Cobalt acetate tetrahydrate (Co(CH₃COO)₂·4H₂O), magnesium acetate tetrahydrate (Mg(CH₃COO)₂·4H₂O) and zinc acetate dihydrate (Zn(CH₃COO)₂·2H₂O) ware obtained from Synth, whereas manganese acetate tetrahydrate (Mn(CH₃COO)₂·4H₂O) was purchased from Carlo Erba.

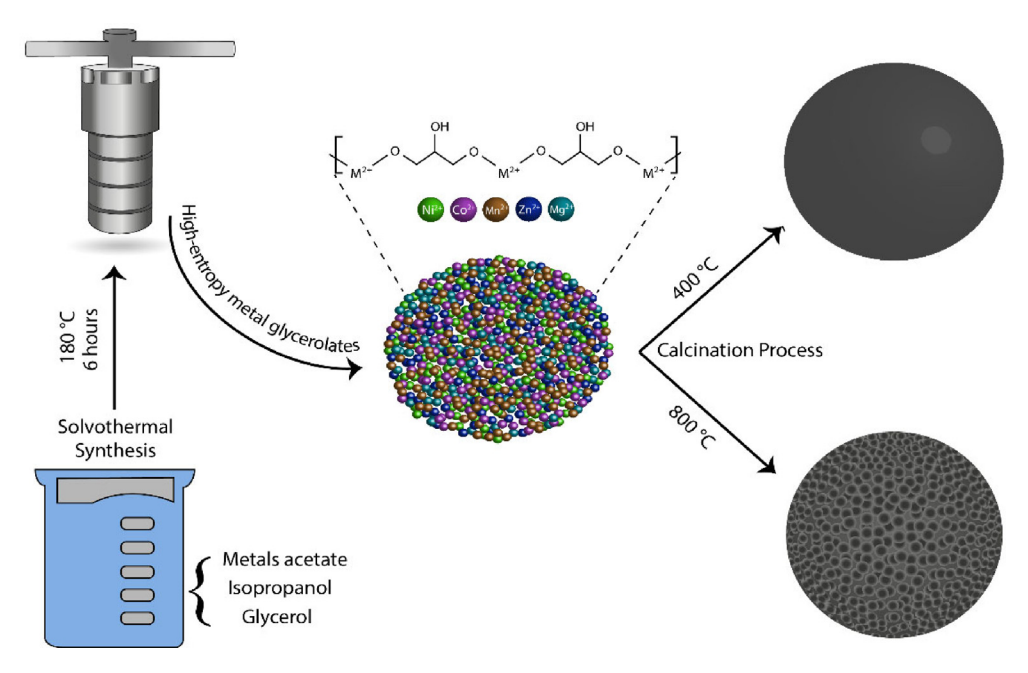
2.2. Materials synthesis

HE-Gly microspheres were obtained by a facile one-step solvothermal method [16,17] (Scheme 1). Typically, equimolar Ni (CH₃COO)₂·4H₂O, Co(CH₃COO)₂·4H₂O, Mn(CH₃COO)₂·4H₂O, Mg (CH₃COO)₂·4H₂O and Zn(CH₃COO)₂·2H₂O (0.5 mmol each) were dissolved in 40 mL isopropanol under continuous stirring for 2 h. Then, 8 mL of glycerol was added to the mixture forming a transparent pink solution after stirring for 30 min. The mixture solution was then transferred to a Teflon-lined stainless-steel autoclave and kept at 180 °C for 10 h. The product (named HE-Gly) was separated by centrifugation, washed with ethanol twice and dried at 60 °C for 10 h. In order to obtain HEO-400 porous microspheres, the assynthesized HE-Gly was annealed at 400 °C in air for 2 h with a heating rate of 2 °C min⁻¹ in a tubular furnace OFT-1200X. On the other hand, HEO-800 was annealed at 800 °C in air for 3 h with a heating rate of 4 °C min⁻¹.

2.3. Characterization

The specimens were characterized by X-ray diffractometry (XRD) in a Bruker D8 Phaser diffractometer using Cu K α source (λ = 1.5418 Å, 40 kV, 40 mA, step = 0.05° with time steps of 1 s), in the 2 θ range from 5° to 90°. Infrared spectra were recorded in a Bruker ALPHA FTIR spectrophotometer. The relative amounts of metals were measured by ICP-OES (Arcos/Spectro) using concentrated dispersions of HE-Gly. Thermogravimetric analysis (TGA) was performed on a Shimadzu TGA Q500 instrument using synthetic air (80% N₂, 20% O₂) flux of 50 mL min⁻¹. Briefly, a specimen was placed in a platinum pan and equilibrated to 35 °C in the TGA prior to the application of a heating ramp of 4 °C min⁻¹ up to 900 °C.

Morphological and high-resolution transmission electron microscopy images were obtained by a JEOL ARM200CF. Energy dispersive spectroscopy (EDS) was performed using an aberration-corrected JEOL ARM200CF with a cold field emission gun operated at 200 kV, equipped with an Oxford X-max 100TLE windowless X-ray detector. Selected area electron diffraction (SAED) analysis of porous HEO microparticles was performed using the same microscope in the TEM diffraction mode with a camera length of 25 cm. For TEM analysis, the synthesized HEMs were dispersed in isopropanol and drop-cast on a lacey carbon copper grid. Scanning electron microscope (SEM) measurements were performed on a 30-kV JEOL JSM-IT500HR. The synthesized HE-Gly



Scheme 1. Schematic of the formation process of HE-Gly and HEO microspheres.

and HEOs with 10 nm platinum/palladium coating were performed using an accelerating voltage of usually 5.0 kV and working distance of 10 mm.

The qualitative chemical analysis of HEO was performed with the help of X-ray photoelectron spectroscopy (XPS). The XPS analysis was performed using a Thermo Scientific ESCALAB 250Xi instrument. The source gun type Al K-alpha at 500 μm spot size in the standard mode was utilized to acquire XPS spectra for individual (Ni, Co, Mn, Mg, Zn, C and O) elements with 0.1 eV energy step resolution.

The specific surface area, pore sizes, and the adsorbed gas volume were determined by nitrogen (N_2) physical adsorption—desorption isotherms using an Adsorption Analyzer Autosorb IQ (Quantachrome Instruments). Before adsorption measurements, specimens were outgassed for 16 h at 150 °C. The specific surface area (SSA) was calculated by using the Brunauer-Emmett-Teller (BET) method, and the pore size distribution was determined by means of nonlinear density functional theory (NLDFT).

3. Results and discussion

To confirm formation of the molecular structure of the precursor high-entropy coordination compound, named HE-Gly, and for its further investigation, the Fourier transform infrared spectroscopy (FTIR) analysis was employed (Figure S1). As expected, the HE-Gly exhibits FTIR spectra with many characteristic bands of organic compounds due to their inherent glycerol moiety [13]. The most intensive and broad band centering at 3440 cm⁻¹ is attributed to the stretching vibrations of hydroxyl groups (O-H) of the glycerolate anions and possible adsorbed glycerol molecules, indicating the presence of non-deprotonated groups. The bands in 2922 and 2851 cm⁻¹, respectively, are assigned to methylene (-CH₂) groups antisymmetric and symmetric C—H stretching modes [18], while the low-intensity IR absorption shoulder at 1350 cm⁻¹ is assigned to the C—H bending vibrations. Several bands appearing between 950 and 1150 cm⁻¹ are assigned to the C-O stretching vibrations [19], and the one at 810 cm⁻¹ is assigned to the outof-plane C—H bending vibrations [13]. Besides, another prominent IR band centering at 590 cm⁻¹ is associated with metal-oxygen

bond (M–O, M = Ni, Co, Mn, Mg and Zn) stretching vibrations, which indicate formation of HE-Gly coordination compound. However, it is also important to note that during the solvothermal reaction, the glycerol can also be oxidized, resulting in formation of compounds containing carboxylate ions, as reported in some previous works [13] and confirmed by the bands (and shoulder) centered at 1430 and 1570 cm⁻¹, which were assigned to the O–C–O stretching vibration modes [20].

As mentioned above, the main characteristics of HEMs is formation of the same phase with random distribution of five or more elements. In this sense, the crystalline structures were first studied using XRD measurements. As expected, HE-Gly presented diffraction peaks at 10.45°, 20.4° (shoulder), 34.7°, and 60°, characteristic of metal-glycerolate that consists of stacked metal-oxygen sheets separated by bonded glycerolate ions [13]. The HEO spheres were obtained by calcination at 400 °C for 2 h (HEO-400) or at 800 °C for 3 h (HEO-800) in air in a tube furnace. After thermal treatment, the diffractogram of the HEO-400 powder reveals broad and low intensity diffraction peaks at 36.2, 43.6, 58.2 and 63.7° indexed as (311), (400), (511) and (440) crystal planes, respectively, corresponding to a product which can be indexed as the spinel $(MgMnCoNiZn)_3O_4$ crystals (Fd-3 m space group) [21,22] (Fig. 1a). No other phases are present, indicating that the HE-Gly precursor is completely converted to HEO spinel phase after the annealing process. On the other hand, HEO-800 exhibited much better defined and intense diffraction peaks characteristic of (111), (220), (311), (222), (400), (422), (511), (440), (620), (533), (622) and (444) diffraction planes representative of the spinel structure at 20 values of 18.5°, 30.4°, 35.9°, 37.6°, 43.6°, 54.2°, 57.8°, 63.5°, 72.1°, 74.7°, 75.2° and 80.4° [21], respectively, as expected for a composite material containing much larger spinel $(MgMnCoNiZn)_3O_4$ crystals (Fd-3 m space group) [21,22]. However, a few other peaks also observed in the diffractogram of HEO-800 specimen, can be attributed to the formation of a second phase based on MgO, as confirmed by the peaks at a 20 of 36.8°, 42.8°, 62.2°, 74.6°, and 78.5° corresponding to (111), (200), (220), (311), and (222) crystallographic planes, respectively, (JCPDS Card No. 45–0946) with a space group of Fm-3 m [23] (Fig. 1a). In fact, Mg ions possess poor compatibility with other transition metals and should be kept at a lower concentration [24].

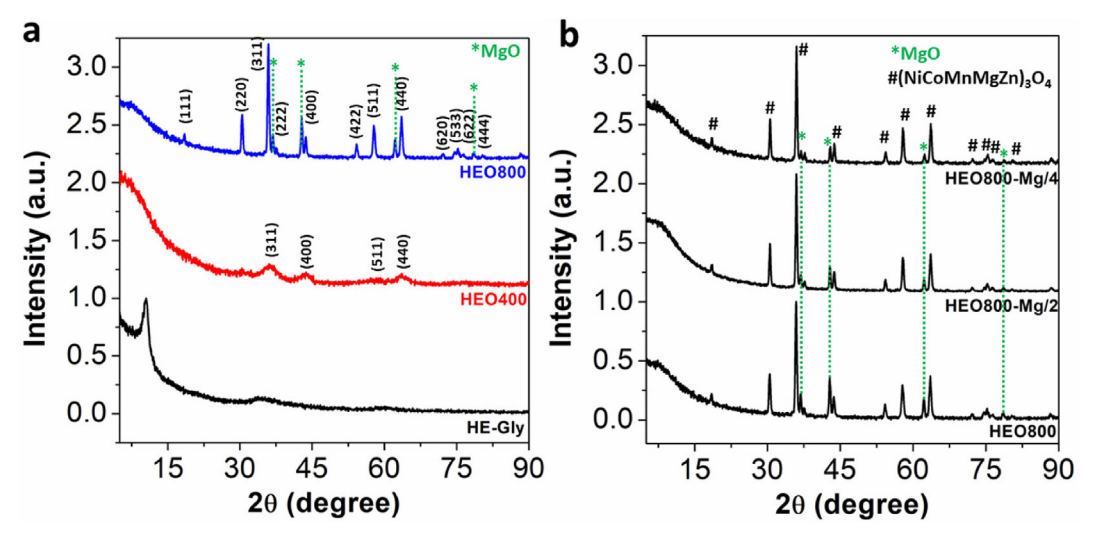


Fig. 1. X-ray diffractograms of (a) HE-Gly, HEO-400 and HEO-800; and (b) HEO-800 prepared by calcination of the HE-Gly precursor with different proportions of Mg²⁺ ions.

Interestingly, that even by means of XRD it is possible to confirm a decrease in the amount of MgO secreted achieved by regulating the amount of Mg in the precursor (HE-Gly) synthesis. For this aim, the amount of all other elements (NiCoMnZn) was maintained, while the amount of magnesium acetate was reduced to one half (named HEO-400-Mg/2) or a quarter (named HEO-400-Mg/4) of the original value. As shown in Fig. 1b, even observing a proportional decrease in the intensities of the peaks attributed to MgO, it is still possible to visualize them when the amount of Mg is four times smaller, indicating an easy segregation of MgO. In fact, MgO is used exclusively in rocksalt and spinel type HEOs to stabilize the structure and thus, ensure the anode electrode cycling stability [25]. For instance, inactive nano-sized MgO particles cause a "spectator effect" to restrain the agglomeration of active nanograins [26]. However, MgO is usually formed after an initial discharge process in the HEO anodes [26]. In this sense, it is important to highlight that in this work, HE-Gly is used as a precursor of spinel oxide phase in a single ex-situ calcination process with the possibility of controlling the amount of MgO present in the HEO, is important in structural stabilization [25], and/or for the implementation [27] and modulation [28] of catalytic sites.

The formation of HEO was also confirmed by TGA, using HE-Gly as a starting material (Figure S2). Usually, the metal coordination compounds (ex. MOF and M-Gly) are thermally unstable and decompose at a temperature below 300 °C to convert to metal oxide in the air. Based on the TGA curve of the HE-Gly precursor in air, four main weight (wt) loss processes can be distinguished. The first step should be related to the gradual removal of the absorbed water and partial oxidative decomposition of the oxygen-enriched organic groups [29] in the inorganic-organic HE-Gly particles with a weight loss of around 27.1%. Between 240 and 275 °C a fast mass loss occurs due to decomposition of glycerolate ligands resulting in a weight loss of ~24.4 wt%. The third stage of mass loss occurs between 275 and 410 very mildly. The slight mass increase from 43.3 to 48.5% between 500 and 900 °C, is probably due to the oxidation process. In fact, the curve is ascending during the oxidation of metal elements in air, which is relatively common for thermal decomposition of coordination compounds, in addition to the presence of carbon residues, even after heating at temperatures as high as 800 °C [30].

The morphology of the as-synthesized HE-Gly particles was examined by TEM (Fig. 2) and SEM (Fig. 3) imaging aiming elucidation of changes in the HEMs morphology induced at the different calcination temperatures. As expected, and in agreement with the

XRD data, the TEM images for the HE-Gly (Fig. 3a) demonstrate microspheres with a relatively low crystallinity, as confirmed by the FFT images and wavy surface (Fig. 3a). Interestingly, HEO-400 has a surface with high porosity, but with still low crystallinity (Fig. 2d-2f and Fig. 3b). It should be emphasized that it is not obvious to visualize the porosity of HEO-400 in Fig. 3b, which is relatively impaired by coating the sample with a 10 nm Pt/Pd film (used to increase conductivity of microparticles). However, in the TEM images (Fig. 2e), it is possible to clearly observe the presence of pores in the HEO-400 sample. On the other hand, the material prepared at 800 °C presented simultaneously high crystallinity (demonstrated in the FFT images, as in Fig. 2i) and microporous structure (displayed in Fig. 2g and Fig. 3c-3f). In fact, the analysis of the selected area electron diffraction (SAED) pattern from the large region of HEO-800 particles supports the results of XRD. It reveals six major diffraction rings indexed as (111), (220), (311), (422), (620), and (444) lattice planes corresponding to the spinel crystal structure (Fig. 4a-4b). Besides, distinct spots could be identified as (200), (220) and (311) planes of MgO in Fig. 4b.Fig. 5..

SEM analysis confirmed that the as-synthesized HE-Gly specimens after calcination treatments possess rough and porous surfaces. Thus, to estimate the specific surface area (SSA), BET analysis was performed, while the non-local density functional theory (NLDFT) was used to determine the size distribution and pore shapes, as well as volume of the adsorbed gas. The SSA and the total pore volume (the latter in given in parentheses) values measured were 342 m 2 g $^{-1}$ (0.164 cm 3 g $^{-1}$), 126 m 2 g $^{-1}$ (0.097 cm 3 g $^{-1}$), and 6.7 m 2 g $^{-1}$ (0.038 cm 3 g $^{-1}$), for the specimens HE-Gly, HEO-400, and HEO-800, respectively. The shape of the hysteresis is dependent on the nature of the material analyzed, as well as the pore sizes present in the structure [31]. In accordance with the N_2 adsorption hysteresis models as reported by IUPAC [32], the HE-Gly specimen possesses the type-I isotherms characteristics of materials with micropores with an average diameter close to 2 nm (Fig. S3a-S3b), while the HEO-400 specimen possesses the type-IV isotherms characteristic of the presence of micro and mesopores (Fig. S3c-S3d). Although the HEO-800 specimen does not present a specific hysteresis, it is possible to observe that the isotherm is no longer almost horizontal behavior near the region $p/p_0 > 0.95$, which is characteristic of the quasi-exclusive absorption in macropores (Fig. S3e-S3f) [32]. The large volume of macropores for the HEO-800 specimen was also clearly revealed by SEM, as discussed earlier. In fact, different rates of adsorption of N2 in the low pres-

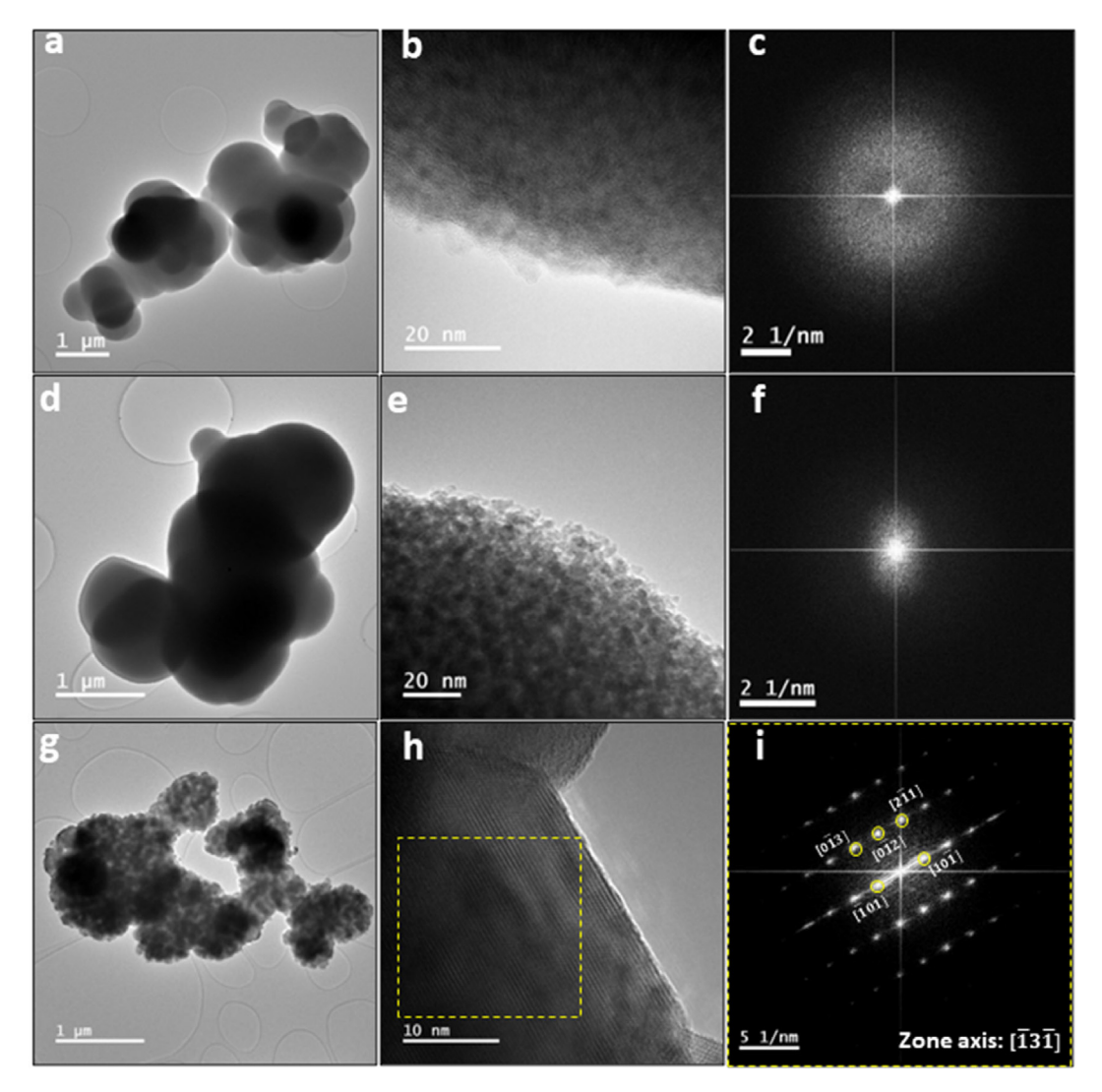


Fig. 2. (a, d, g) Low-magnification TEM micrograph, (b, e, g) high-magnification TEM micrograph and (c, f, i) their respective FFT images of (a-c) HE-Gly, (d-f) HEO-400 and (g-i) HEO-800.

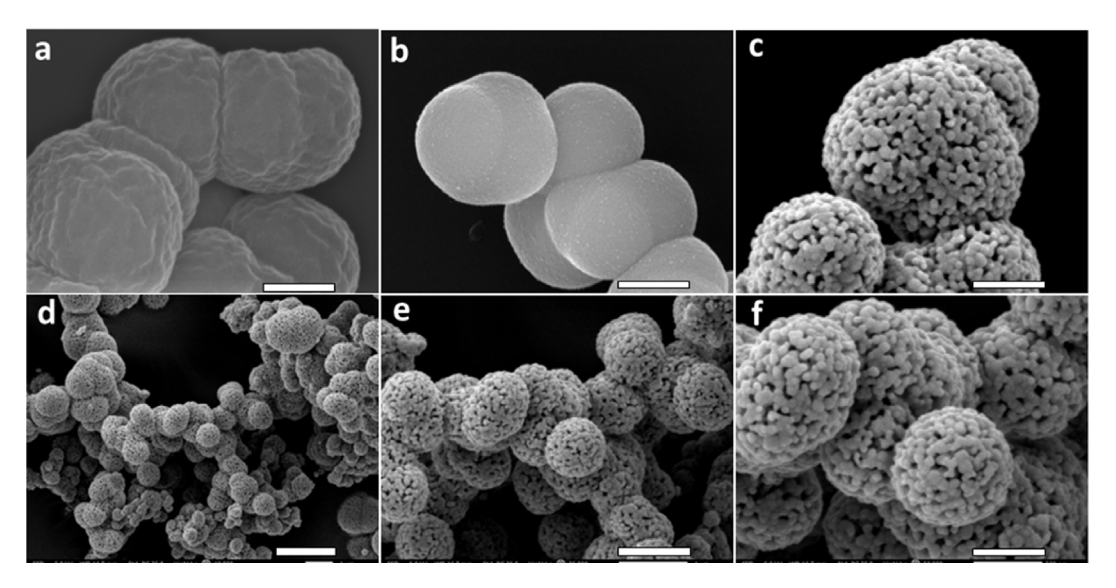


Fig. 3. SEM images, which show microspheres of (a) HE-Gly, (b) HEO-400, and (c) HEO-800. (Scale bar corresponds to 500 nm). SEM images, which reveal microspheres of HEO-800 at different magnification: (d) \times 10.000, (e) \times 25.000, and (f) \times 50.000.

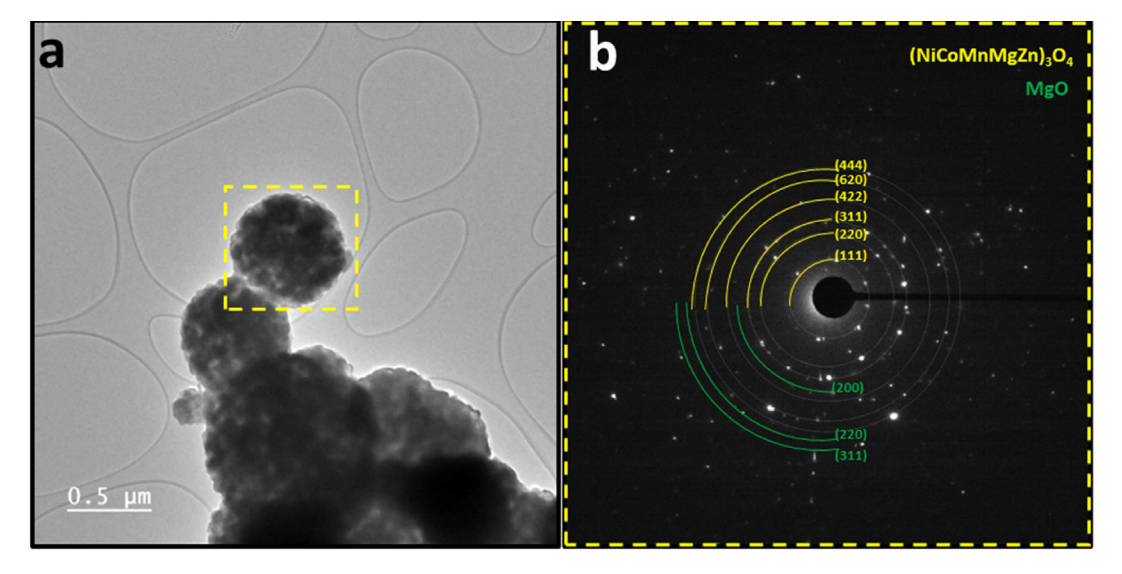


Fig. 4. (a) TEM image of HEO specimens synthesized at 800 °C, and (b) SAED analysis confirming the spinel crystal structure.

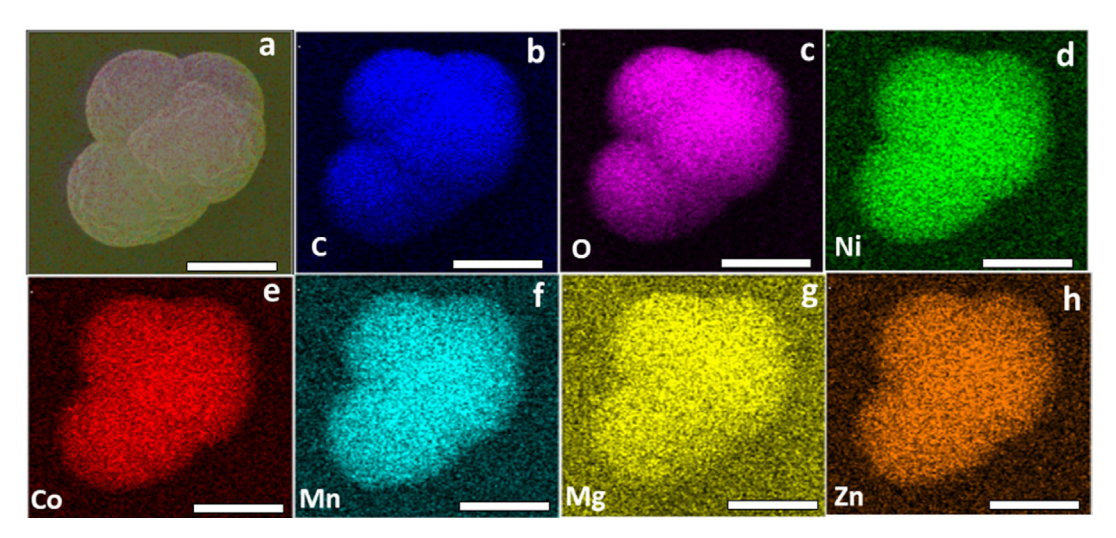


Fig. 5. SEM-EDS analysis of HE-Gly particles. (a) EDS overlap mapping of HE-Gly particles (scale bar is 500 nm). EDS elemental mapping of individual elements constituting HE-Gly particles indicating the high mixing entropy. All scale bars correspond to 500 nm. (b) carbon (blue), (c) oxygen (magenta), (d) nickel (green), (e) cobalt (red), (f) manganese (light blue), (g) magnesium (yellow), and (h) zinc (orange). (For interpretation of the references to colour in this figure legend, the reader is referred to the web version of this article.)

sure region (p/p₀ < 0.01, **Figure S4**) for each sample, are characteristic of the presence of micropores [33]. According to the results obtained by BET/NLDFT, the specimens revealed a hierarchical porous structure, which is dependent on their calcination temperature. For instance, the high SSA of the HE-Gly specimen can be attributed to the significant amount of micropores, as highlighted in Fig. S3b, as well as to its rough surface (in this case, revealed by SEM images). The HEO-400 specimen reveals a significant decrease in the amount of micropores. However, mesopores with an average size of \sim 3.5 nm are revealed (Fig. S3d), which can be attributed to the beginning of the ordering of the material at the calcination temperature of 400 °C.

The SEM-EDS analysis demonstrates that the cations are distributed homogeneously across the HE-Gly particles (Fig. 2d), which confirms formation of a high-entropy coordination compound. The elemental concentrations are 20.10, 20.53, 19.70, 19.63, and 20.04% for Ni, Co, Mn, Mg and Zn; respectively, as obtained from the EDS analysis (Figure S5). Furthermore, to confirm the nearly equimolar metal concentrations of HE-Gly precursor, an ICP-OES measurement was performed, which

revealed 20.06, 21.80, 21.22, 18.87, and 18.05% for Ni, Co, Mn, Mg and Zn; respectively.

The prepared HEOs were also characterized by SEM-EDS (Fig. 6). Similarly, the representative EDS mapping images for both types of HEO demonstrate almost uniform distribution of Ni, Co, Mn, Mg and Zn, indicating that the chemical homogeneity at this degree of magnification is very close to equimolar composition used in the HE-Gly precursors. Moreover, the EDS results displayed in Table 1 reveal a slight deviation especially for the percentages of Mg, which may be due to the presence of secreted MgO nanoparticles (Figure S6 and S7). In fact, in the EDS-TEM overlap mapping at higher magnification it is possible to visualize regions with different shades which manifest different concentrations of the metallic components (Fig. 7), as expected for a material with phase segregation (Figure S8).

The XPS measurement was also carried out to investigate the surface elemental composition and chemical state of HE-Gly and HEOs specimens. The precursor material, HE-Gly, reveals At% surface of carbon approximately 6 times higher than that for HEOs (Table 2 and Figure S9) and a superior oxygen At%, as expected for

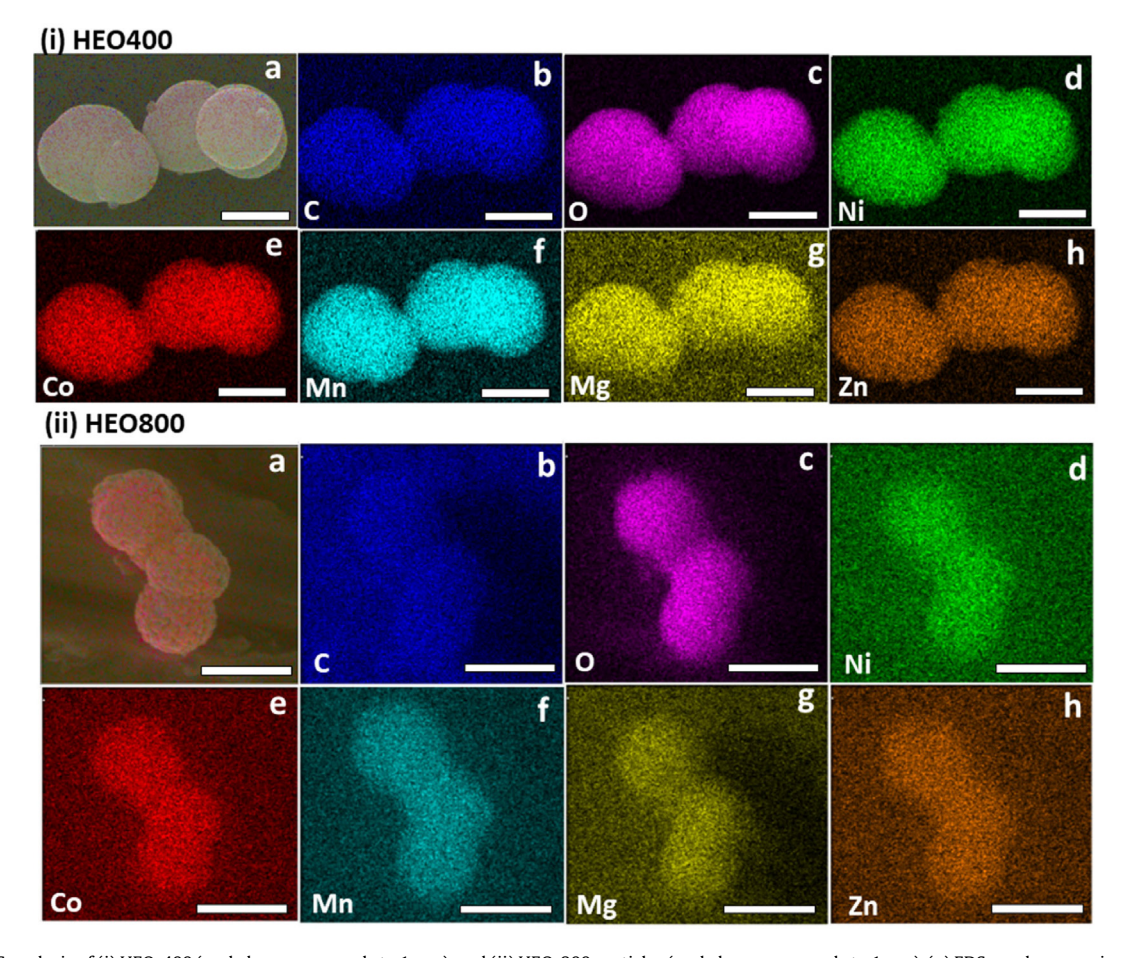


Fig. 6. SEM-EDS analysis of (i) HEO-400 (scale bar corresponds to 1 μm), and (ii) HEO-800 particles (scale bar corresponds to 1 μm). (a) EDS overlap mapping of HEO particles. EDS elemental mapping of individual elements constituting HEO particles indicating the high mixing entropy. (b) carbon (blue), (c) oxygen (magenta), (d) nickel (green), (e) cobalt (red), (f) manganese (light blue), (g) magnesium (yellow), and (h) zinc (orange). (For interpretation of the references to colour in this figure legend, the reader is referred to the web version of this article.)

Table 1Chemical composition (atomic %) obtained from the energy dispersive spectroscopy (EDS).

Specimens	Ni (At%)	Co (At%)	Mn (At%)	Mg (At%)	Zn (At%)
HE-Gly	20.10	20.53	19.70	19.63	20.04
HEO-400	19.02	19.60	19.78	22.38	19.22
HEO-800	21.19	21.07	21.57	15.84	20.33

a coordination compound containing organic ligands. Another important information obtained from the survey spectra is the higher At% of $\mathrm{Mg^{2^+}}$ ions at the microsphere surface after the annealing process. In fact, during the annealing process in air, the oxidation of glycerolate and/or metal ions would happen first at the surface of the HE-Gly precursor with the thermodynamically favorable formation of MgO at this initial stage, especially due to the low value of $\Delta G_{\rm f}^{\rm o}$ (-569.43 kJ $\rm mol^{-1}$) compared to other metal monoxides (**Table S1**), as also confirmed by the XRD results. At the next step at high temperature there is formation of spinel HEO phase and crystallization of the secreted phase of MgO. Then, with continuous evacuation of the core HE-Gly material to the surface for reaction with oxygen in air, inner cavities would eventually form and result in formation of hollow microspheres [34].

To obtain the valence states of different elements in a HE-compound, the high resolution XPS spectra were obtained, as shown in Fig. 8. Fig. 8a depicts the high-resolution XPS Ni 2p spectrum of HE-Gly which reveals two valence states of Ni²⁺ and Ni³⁺. The peaks of Ni 2p_{3/2} and Ni 2p_{1/2} are located at 854.6 and

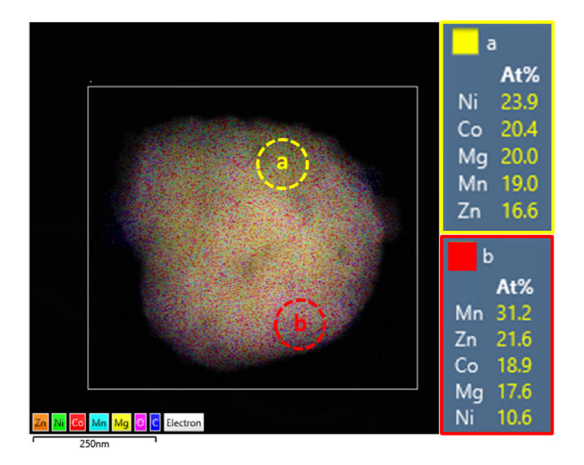


Fig. 7. TEM-EDS overlap mapping of HEO-800 particle (scale bar corresponds to 250 nm). Carbon (blue), oxygen (magenta), nickel (green), cobalt (red), manganese (light blue), magnesium (yellow) and zinc (orange). (For interpretation of the references to colour in this figure legend, the reader is referred to the web version of this article.)

Table 2
Chemical composition (atomic %) obtained from X-ray photoelectron spectroscopy (XPS).

Specimens	Ni (At%)	Co (At%)	Mn (At%)	Mg (At%)	Zn (At%)	O (At%)	C (At%)	O/M
HE-Gly	3.62	4.65	3.21	6.08	7.61	41.14	33.7	1.63
HEO-400	7.55	10.12	14.51	15.59	14.55	32.57	5.11	0.52
HEO-800	6.74	7.27	12.53	18.15	11.10	38.29	5.92	0.69

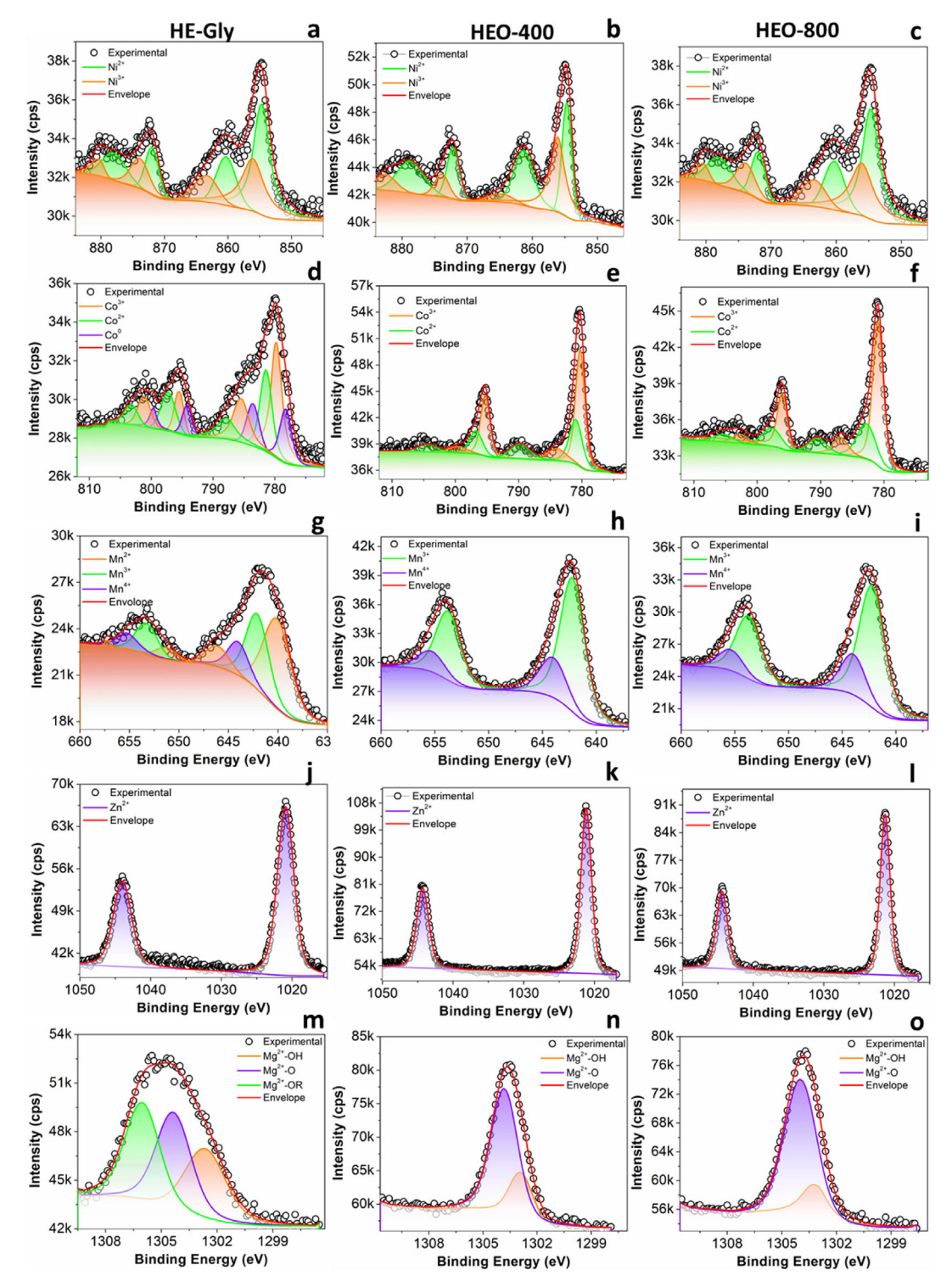


Fig. 8. High-resolution XPS spectra for HE-GLy, HEO-400 and HEO-800: (a-c) Ni 2p, (d-f) Co 2p, (g-i) Mn 2p, (j-l) Zn 2p and (m-o) Mg 1s.

871.9 eV for Ni²⁺, respectively, while Ni³⁺ peaks are seen at 856.0 eV (Ni $2p_{3/2}$) and 873.9 eV (Ni $2p_{1/2}$), respectively. Foursatellite peaks are also seen in the Ni 2p spectrum. Similarly to Ni 2p, the spectrum of Co 2p also reveals the oxidation of part of Co^{2+} ions. In fact, the Co 2p spectrum shows $Co^{2+}(Co 2p_{3/2})$ and $Co^{3+}(Co\ 2p_{3/2})$ at 781.4 and 779.7 eV, respectively, and $Co^{2+}(Co\ 2p_{3/2})$ $2p_{1/2}$) and Co^{3+} (Co $2p_{1/2}$) at 796.4 and 795.0 eV, respectively. Four main satellite peaks at 785.5, 787.7, 800.4 and 803.2 eV were found. Interestingly, the Co 2p spectrum for HE-Gly precursor also demonstrates the possibility of metallic Co⁰ formation, as evidenced by two low-intensity shoulders at 778.2 and 793.8 eV [35] and two more satellite peaks at 783.6 and 798.0 eV. At this point it is important to mention that glycerol has also been used as a reducing agent in the design of Co or AgCo nanoparticles [36,37]. The deconvolution of the Mn 2p spectrum reveals a broad Mn 2p_{3/2} peak that suggests partial oxidation of Mn²⁺ ions, as confirmed by the contribution of Mn²⁺, Mn³⁺, and Mn⁴⁺ ions at 640.1, 641.2, and 644.4 eV, respectively. The Mn $2p_{1/2}$ peak was also deconvoluted into three peaks, which are Mn²⁺ at 651.4 eV, Mn³⁺ at 653.4 eV, and Mn⁴⁺ at 655.3 eV. The peaks at 646.5 and 657.7 eV are satellite peaks. As usual, the Zn 2p spectrum reveals only one valence state corresponding to Zn2+ with two peaks at 1020.9 eV and 1044.0 eV belonging to Zn 2p_{3/2} and Zn 2p_{1/2}, respectively. Furthermore, the broad Mg 1s spectrum was deconvoluted into three components corresponding to Mg²⁺ which can be assigned to Mg-OH, Mg-O and Mg-OR at 1302.6, 1304.3 and 1306.0 eV, respectively. The O 1s spectrum (Figure S10d-S10f) were deconvoluted into four oxygen components, M-O, OH-, C-O, and physically absorbed H₂O at 529.3, 530.0, 531.4, 533.0 eV, respectively [13,19]. The partial oxidation of glycerol after the solvothermal reaction can be also observed in the C 1s spectrum which reveals peaks at 283.6, 284.4, 285.5, and 287.6 eV attributed to the C=C, C-C, C-O, and O-C=O bonding, respectively (Figure S10a-S10c).

After the calcination process at 400 or 800 °C, the high-resolution XPS spectra reveal significant changes for some of the metal ions. For instance, the Mn 2p spectra for HEO-400 and HEO-800 reveal total oxidation of $\rm Mn^{2+}$ ions to $\rm Mn^{3+}$ and $\rm Mn^{4+}$. Another main spectral difference can be observed especially for Mg²+ ions which clearly demonstrates the absence of the peak at 1306.0 eV as expected by the loss of the lamellar structure of HE-Gly and formation of the respective HEO. Interestingly, the amount of Ni³+ decreases in the following order, HE-Gly, HEO-400 and HEO-800, as the calcination temperature increases, while the At% of Co³+ increases following the same order of the materials described above (HE-Gly < HEO-400 < HEO-800).

4. Conclusion

For the first time, we demonstrated a scalable solvothermal approach for the synthesis of metal glycerolate-based high entropy microparticles that could be converted into porous HEO microparticles by the annealing process. The HE-Gly microparticles containing five metals, such as Ni, Co, Mn, Zn and Mg were synthesized. The morphological and structural characterizations demonstrate that the temperature of the annealing process plays an important role in development of porosity and crystallinity of the prepared HEOs. The Mg-containing HE-Gly results in porous HEOs with MgO secreted after the annealing process at 800 °C. The amount of MgO is controlled by adjusting the salt concentration used in the solvothermal synthesis. The result demonstrates a viable strategy that leads to development of new HE-Gly, and HEOs materials with a much higher metal concentration, variable crystallinity and modulable porous structures, opening a new avenue to explore novel, outstanding high-entropy materials for various applications.

CRediT authorship contribution statement

Josué M. Gonçalves: Conceptualization, Methodology, Formal analysis, Investigation, Visualization, Writing – review & editing. Alireza Ghorbani: Investigation, Writing – original draft. Timothy G. Ritter: Investigation, Writing – original draft. Irlan S. Lima: Investigation, Writing – original draft. Mahmoud Tamadoni Saray: Investigation, Writing – original draft. Abhijit H. Phakatkar: Investigation, Writing – original draft. Vinicius D. Silva: Investigation, Writing – original draft. Rafael S. Pereira: Investigation, Formal analysis. Alexander L. Yarin: Resources, Writing – review & editing. Lúcio Angnes: Conceptualization, Resources, Writing – review & editing, Funding acquisition. Reza Shahbazian-Yassar: Conceptualization, Resources, Writing – review & editing, Funding acquisition.

Data availability

Data will be made available on request.

Declaration of Competing Interest

The authors declare that they have no known competing financial interests or personal relationships that could have appeared to influence the work reported in this paper.

Acknowledgments

The authors acknowledge financial support from National Science Foundation DMR- 1809439, Brazilian agencies for their support: FAPESP (grant numbers: 2018/16896-7 and projects 2017/13137-5) and CNPq (grant numbers: 311847-2018-8 and project 465389/2014-7). In addition, we thank the fellowship granted to J.M.G. (FAPESP 2020/06176-7), I.S.L. (FAPESP 2022/04127-4) and V.D.S. (CNPq 202290/2020-4). This work made use of Instruments in the Electron Microscopy Core (Research Resources Center, UIC). We thank Prof. Koiti Araki (Laboratório de Química Supramolecular e Nanotecnologia, IQ-USP) and Sis-NANO USP for the use of TGA and FTIR spectroscopy facility. This work made use of the Keck-II facility of Northwestern University's NUANCE Center – Dr. Xingi Chen, which has received support from the Soft and Hybrid Nanotechnology Experimental (SHyNE) Resource (NSF ECCS-1542205), the MRSEC program (NSF DMR-1720139) at the Materials Research Center.

Appendix A. Supplementary data

Supplementary data to this article can be found online at https://doi.org/10.1016/j.jcis.2023.03.089.

References

- [1] D. Luo, Q. Zhou, Z. Huang, Y. Li, Y. Liu, Q. Li, Y. He, H. Wang, Tribological Behavior of High Entropy Alloy Coatings: A Review, Coatings 12 (2022) 1428, https://doi.org/10.3390/coatings12101428.
- [2] D. Luo, Q. Zhou, W. Ye, Y. Ren, C. Greiner, Y. He, H. Wang, Design and Characterization of Self-Lubricating Refractory High Entropy Alloy-Based Multilayered Films, Acs Appl Mater Inter 13 (2021) 55712–55725, https://doi.org/10.1021/acsami.1c16949.
- [3] J. Feng, Y. Tang, J. Liu, P. Zhang, C. Liu, L. Wang, Bio-high entropy alloys: Progress, challenges, and opportunities, Front. Bioeng. Biotechnol. 10 (2022). https://www.frontiersin.org/articles/10.3389/fbioe.2022.977282 977282.
- [4] V.R. Naganaboina, M. Anandkumar, A.S. Deshpande, S.G. Singh, Single-phase high-entropy oxide-based chemiresistor: Toward selective and sensitive detection of methane gas for real-time applications, Sens. Actuators B Chem. 357 (2022). https://www.sciencedirect.com/science/article/pii/ S0925400522000685 131426.

- [5] K. Wang, J. Huang, H. Chen, Y. Wang, W. Yan, X. Yuan, S. Song, J. Zhang, X. Sun, Recent Progress in High Entropy Alloys for Electrocatalysts, Electrochem. Energy Rev. 5 (2022) 17, https://doi.org/10.1007/s41918-022-00144-8.
- [6] A. Amiri, R. Shahbazian-Yassar, Recent progress of high-entropy materials for energy storage and conversion, J Mater Chem A 9 (2021) 782–823, https://doi. org/10.1039/D0TA09578H.
- [7] A. Sarkar, L. Velasco, D. Wang, Q. Wang, G. Talasila, L. de Biasi, C. Kübel, T. Brezesinski, S.S. Bhattacharya, H. Hahn, B. Breitung, High entropy oxides for reversible energy storage, Nat. Commun. 9 (2018) 3400, https://doi.org/10.1038/s41467-018-05774-5.
- [8] T.G. Ritter, A.H. Phakatkar, M.G. Rasul, M.T. Saray, L.V. Sorokina, T. Shokuhfar, J. M. Gonçalves, R. Shahbazian-Yassar, Electrochemical synthesis of high entropy hydroxides and oxides boosted by hydrogen evolution reaction, Cell Rep. Phys. Sci. 3 (2022). https://www.sciencedirect.com/science/article/pii/S2666386422001217 100847.
- [9] Q. Wang, A. Sarkar, D. Wang, L. Velasco, R. Azmi, S.S. Bhattacharya, T. Bergfeldt, A. Düvel, P. Heitjans, T. Brezesinski, H. Hahn, B. Breitung, Multi-anionic and cationic compounds: new high entropy materials for advanced Li-ion batteries, Energ. Environ Sci 12 (2019) 2433–2442, https://doi.org/10.1039/C9EE00368A.
- [10] Y. Ma, Y. Ma, S.L. Dreyer, Q. Wang, K. Wang, D. Goonetilleke, A. Omar, D. Mikhailova, H. Hahn, B. Breitung, T. Brezesinski, High-Entropy Metal-Organic Frameworks for Highly Reversible Sodium Storage, Adv Mater 33 (2021) 2101342, https://doi.org/10.1002/adma.202101342.
- [11] X. Zhao, Z. Xue, W. Chen, X. Bai, R. Shi, T. Mu, Ambient fast, large-scale synthesis of entropy-stabilized metal-organic framework nanosheets for electrocatalytic oxygen evolution, J Mater Chem A 7 (2019) 26238–26242, https://doi.org/10.1039/C9TA09975A.
- [12] J.M. Gonçalves, A.L. Hennemann, J.G. Ruiz-Montoya, P.R. Martins, K. Araki, L. Angnes, R. Shahbazian-Yassar, Metal-glycerolates and their derivatives as electrode materials: A review on recent developments, challenges, and future perspectives, Coord. Chem. Rev. 477 (2023). https://www.sciencedirect.com/science/article/pii/S0010854522005495 214954.
- [13] T.X. Nguyen, Y.-H. Su, C.-C. Lin, J. Ruan, J.-M. Ting, A New High Entropy Glycerate for High Performance Oxygen Evolution Reaction, Adv. Sci. 8 (2021) 2002446, https://doi.org/10.1002/advs.202002446.
- [14] J.M. Gonçalves, P.R. Martins, D.P. Rocha, T.A. Matias, M.S.S. Julião, R.A.A. Munoz, L. Angnes, Recent trends and perspectives in electrochemical sensors based on MOF-derived materials, J Mater Chem C 9 (2021) 8718–8745, https://doi.org/10.1039/D1TC02025K.
- [15] Y. Zheng, H. Geng, Y. Zhang, L. Chen, C.C. Li, Precursor-Based Synthesis of Porous Colloidal Particles towards Highly Efficient Catalysts, Chem. Eur. J. 24 (2018) 10280–10290, https://doi.org/10.1002/chem.201800625.
- [16] L. Zhu, H. Lu, F. Xiao, T. Yao, T. Liu, F. Li, J. Wang, X. Han, Y. Cheng, H. Wang, Flower-like Mn/Co Glycerolate-Derived α-MnS/Co9S8/Carbon Heterostructures for High-Performance Lithium-Ion Batteries, ACS Appl. Energy Mater. 3 (2020) 10215–10223, https://doi.org/10.1021/acsaem.0c02014.
- [17] M. Wang, J. Jiang, L. Ai, Layered Bimetallic Iron-Nickel Alkoxide Microspheres as High-Performance Electrocatalysts for Oxygen Evolution Reaction in Alkaline Media, Acs Sustain. Chem. Eng. 6 (2018) 6117–6125, https://doi.org/ 10.1021/acssuschemeng,7b04784.
- [18] J.M. Goncalves, R.R. Guimaraes, C.V. Nunes, A. Duarte, B.B.N.S. Brandao, H.E. Toma, K. Araki, Electrode materials based on alpha-NiCo(OH)₂ and rGO for high performance energy storage devices, Rsc Adv 6 (2016) 102504–102512, https://doi.org/10.1039/C6RA20317E.
- [19] N.-H. Ting, T.X. Nguyen, C.-H. Lee, Y.-C. Chen, C.-H. Yeh, H.-Y.-T. Chen, J.-M. Ting, Composition-controlled high entropy metal glycerate as high-performance electrocatalyst for oxygen evolution reaction, Appl. Mater. Today 27 (2022). https://www.sciencedirect.com/science/article/pii/S2352940722000373 101398.
- [20] J.F. Gomes, A.C. Garcia, L.H.S. Gasparotto, N.E. de Souza, E.B. Ferreira, C. Pires, G. Tremiliosi-Filho, Influence of silver on the glycerol electro-oxidation over AuAg/C catalysts in alkaline medium: a cyclic voltammetry and in situ FTIR spectroscopy study, Electrochim. Acta 144 (2014) 361–368. https://www.sciencedirect.com/science/article/pii/S0013468614016582.
- [21] D. Wang, S. Jiang, C. Duan, J. Mao, Y. Dong, K. Dong, Z. Wang, S. Luo, Y. Liu, X. Qi, Spinel-structured high entropy oxide (FeCoNiCrMn)304 as anode towards

- superior lithium storage performance, J. Alloy Compd 844 (2020). https://www.sciencedirect.com/science/article/pii/S0925838820325226 156158.
- [22] A. Mao, F. Quan, H.-Z. Xiang, Z.-G. Zhang, K. Kuramoto, A.-L. Xia, Facile synthesis and ferrimagnetic property of spinel (CoCrFeMnNi)304 high-entropy oxide nanocrystalline powder, J Mol Struct 1194 (2019) 11–18. https://www.sciencedirect.com/science/article/pii/S002228601930643X.
- https://www.sciencedirect.com/science/article/pii/S002228601930643X.

 [23] T.D. Desissa, M. Meja, D. Andoshe, F. Olu, F. Gochole, G. Bekele, O.A. Zelekew, T. Temesgen, B. Brehane, K.D. Kuffi, T. Hunde, Synthesis and characterizations of (Mg Co, Ni, Cu, Zn)O high-entropy oxides, SN Appl. Sci. 3 (2021) 733, https://doi.org/10.1007/s42452-021-04724-z.
- [24] X. Liu, X. Li, Y. Li, H. Zhang, Q. Jia, S. Zhang, W. Lei, High-entropy oxide: A future anode contender for lithium-ion battery, EcoMat, n/a (2022) e12261. https://doi.org/10.1002/eom2.12261.
- [25] T.X. Nguyen, J. Patra, J.-K. Chang, J.-M. Ting, High entropy spinel oxide nanoparticles for superior lithiation-delithiation performance, J Mater Chem A 8 (2020) 18963–18973, https://doi.org/10.1039/D0TA04844E.
- [26] N. Qiu, H. Chen, Z. Yang, S. Sun, Y. Wang, Y. Cui, A high entropy oxide (Mg0.2Co0.2Ni0.2Cu0.2Zn0.20) with superior lithium storage performance, J Alloy Compd 777 (2019) 767–774. https://www.sciencedirect.com/science/ article/pii/S0925838818341677.
- [27] I. Reyero, G. Arzamendi, L.M. Gandía, Heterogenization of the biodiesel synthesis catalysis: CaO and novel calcium compounds as transesterification catalysts, Chem. Eng. Res. Des. 92 (2014) 1519–1530. https:// www.sciencedirect.com/science/article/pii/S026387621300508X.
- [28] Y. Zhang, Z. Zhang, G. Jiang, A.H. Mamaghani, S. Sy, R. Gao, Y. Jiang, Y. Deng, Z. Bai, L. Yang, A. Yu, Z. Chen, Three-dimensionally ordered mesoporous Co3O4 decorated with Mg as bifunctional oxygen electrocatalysts for high-performance zinc-air batteries, Nano Energy 100 (2022). https://www.sciencedirect.com/science/article/pii/S2211285522005031 107425.
- [29] Z. Wang, D.K. Denis, Z. Zhao, X. Sun, J. Zhang, L. Hou, C. Yuan, Unusual formation of hollow NiCoO2 sub-microspheres by oxygen functional group dominated thermally induced mass relocation towards efficient lithium storage, J Mater Chem A 7 (2019) 18109–18117, https://doi.org/10.1039/ C9TA064321
- [30] X.-N. Lv, P.-F. Wang, Y.-H. Zhang, Q. Shi, F.-N. Shi, MOF-derived CoFe204/FeO/Fe nanocomposites as anode materials for high-performance lithium-ion batteries, J Alloy Compd (2022). https://www.sciencedirect.com/science/article/pii/S0925838822027074 166316.
- [31] R. Bardestani, G.S. Patience, S. Kaliaguine, Experimental methods in chemical engineering: specific surface area and pore size distribution measurements— BET, BJH, and DFT, Can. J. Chem. Eng. 97 (2019) 2781–2791, https://doi.org/ 10.1002/cjce.23632.
- [32] M. Thommes, K. Kaneko, A.V. Neimark, J.P. Olivier, F. Rodriguez-Reinoso, J. Rouquerol, K.S.W. Sing, Physisorption of gases, with special reference to the evaluation of surface area and pore size distribution (IUPAC, Technical Report) 87 (2015) 1051–1069, https://doi.org/10.1515/pac-2014-1117.
- [33] A. Noparvar-Qarebagh, H. Roghani-Mamaqani, M. Salami-Kalajahi, Novolac phenolic resin and graphene aerogel organic-inorganic nanohybrids: High carbon yields by resin modification and its incorporation into aerogel network, Polym. Degrad. Stab. 124 (2016) 1–14. https:// www.sciencedirect.com/science/article/pii/S0141391015301464.
- [34] W. Du, R. Liu, Y. Jiang, Q. Lu, Y. Fan, F. Gao, Facile synthesis of hollow Co3O4 boxes for high capacity supercapacitor, J Power Sources 227 (2013) 101–105. https://www.sciencedirect.com/science/article/pii/S0378775312016825.
- [35] Y.T. Law, T. Dintzer, S. Zafeiratos, Surface oxidation of NiCo alloy: A comparative X-ray photoelectron spectroscopy study in a wide pressure range, Appl Surf Sci 258 (2011) 1480–1487. https:// www.sciencedirect.com/science/article/pii/S0169433211015145.
- [36] J.A. Adekoya, S. Mlowe, E.O. Dare, M.A. Mesubi, N. Revaprasadu, Synthesis and characterization of polyol stabilised Ag/Co allied nanocomposites, Superlattice. Microst. 78 (2015) 97–105. https:// www.sciencedirect.com/science/article/pii/S074960361400456X.
- [37] L. Duan, S. Jia, L. Zhao, Study on morphologies of Co microcrystals produced by solvothermal method with different solvents, Mater Res Bull 45 (2010) 373– 376. https://www.sciencedirect.com/science/article/pii/ S002554081000005X.